Journal of *Marine Science and Engineering*

MDPI

*Article*

# Experiment Tests and Numerical Simulations of Leakage from Double-Hull Oil Tanks in a Fixed State

**Wenzhuo Zhang, Renqing Zhu, Xinlong Zhang *, Qingyi Qu and Hui Zhao**

School of Naval Architecture and Ocean Engineering, Jiangsu University of Science and Technology, Zhenjiang 212100, China; 231210101230@stu.just.edu.cn (W.Z.)
* Correspondence: just.zhangxinlong@just.edu.cn

**Abstract**

To investigate the leakage characteristics of damaged double-hull oil tanks in still water, this study conducted both model tests and numerical simulations on the leakage process of a damaged double-hull oil tank model. Based on a 75,000 DWT oil tanker, a scaled model was designed according to similarity criteria. The effects of different damaged locations (side-shell and bottom) and various breach sizes on the tank's leakage behavior were examined. The evolution of multiphase flow inside the tank and the surrounding flow field was captured, and the leakage pressure under fixed model conditions was measured. The model test results indicate that larger breach sizes lead to a more rapid stabilization of the pressure load during leakage and the liquid exchange process. For side shell breaches, after an initial phase of pressure-difference-driven leakage, a density-driven flow develops at the stable liquid interface. Bottom breaches cause flooding that results in an oil sealing phenomenon at the bottom, leading to a pronounced oil–water stratification. Corresponding numerical simulations of the model tests were performed, and the results were compared and validated against the model test data.

**Keywords:** tank sloshing; damaged oil tank; model test; multiphase flow

## 1. Introduction

### *1.1. Background*

Liquid-carrying vessels may suffer damage to the side shell or bottom due to grounding, collision, and other accidents, which can lead to complex fluid motions, such as flooding, leakage, and sloshing. These phenomena may further affect the structural performance and navigational safety of the vessel. Although the shipping industry has seen an overall decline in accidents and losses with the establishment, refinement, and strict enforcement of various regulations and conventions, statistics from ESMA (2021) [1] on ship casualty data indicate that collisions and damage-induced flooding/leakage still account for over 50% of maritime incidents. The process of flooding and leakage following hull breach involves intricate flow field motions and coupling effects. Both the sloshing of liquid inside the tank and the fluctuating external flow field exhibit strongly nonlinear characteristics, undoubtedly posing challenges for theoretical analysis and numerical simulation. Model testing and numerical simulation methods provide an intuitive and practical means to study the coupled interactions between damage-induced flooding/leakage and liquid sloshing in tanks.

Check for updates

Academic Editor: Eugen Rusu

Received: 12 January 2026
Revised: 19 February 2026
Accepted: 20 February 2026
Published: 24 February 2026

**Copyright:** © 2026 by the authors. Licensee MDPI, Basel, Switzerland. This article is an open access article distributed under the terms and conditions of the Creative Commons Attribution (CC BY) license.

### 1.2. Literature Review

#### 1.2.1. Empty Compartment

(a) Theoretical research

Zaraphonitis et al. (1997) [2] proposed a concentrated mass-spring model. This method assumes that the free surface inside the liquid tank remains stationary throughout the ship's motion and leakage-induced flooding process. However, it treats the liquid volume in the tank as a mass block, which is connected to the hull via springs to simulate slamming forces and motion damping exerted on the hull during water ingress. Fthenakis V.M. (1999) [3] developed a model based on fluid mechanics to determine leakage resulting from variations in gravity and pressure, demonstrating that such variations are caused by the motion of the container or fluctuations of the free surface.

(b) Model test

Santos (2002) [4] developed a model describing ship motion and damaged compartment flooding, and the model tests results showed good agreement with theoretical predictions, demonstrating that asymmetric flooding can lead to capsizing of ro-ro vessels. Zhang et al. (2013) [5] conducted model test studies on ship models with both side-shell and bottom breaches to simulate the dynamic flooding process of damaged compartments, and the results were compared and validated against numerical simulations. Siddiqui (2020) [6] performed experiments on damaged ship compartments under wave conditions, investigating the influence of flooding and sloshing on the natural roll period and roll damping of the vessel under various wave scenarios. Liu WB (2023) [7] designed a three-compartment test model and measured the motion response of a flooding ship under different ventilation opening areas.

(c) Numerical simulation

Papanikolaou (2000) [8] assumed that the water mass was concentrated at its centroid and simulated the flooding-induced capsizing process of a ro-ro vessel, establishing a coupled model of ship motion and damaged-compartment flooding. Jasionowski A. (2001) [9] developed a numerical program for simulating ship motion by integrating the wetted surface area of the hull to obtain nonlinear wave excitation forces, while simplifying the flow motion inside the compartments, to study the dynamic response of a damaged hull. Gao Qiuxin (2001) [10] applied the RANS equations to simulate the flooding of a damaged ship. The volume of fluid (VOF) method was employed to handle the turbulent flow near the free surface, capturing the fundamental flow characteristics associated with ship damage. Fujiwara (2005) [11] applied a two-dimensional lumped-mass concept to numerically simulate the water-on-deck scenario of a ro-ro vessel and validated its effectiveness. Pekka Ruponen (2007) [12] applied a pressure-correction technique for the numerical simulation of compartment flooding. Based on ideal fluid mechanics, the hydrostatic pressure was determined from the water depth to maintain a horizontal free surface. The study focused on compartment flooding and air pressure distribution. Valanto (2008) [13] employed a concentrated mass-spring model to investigate the ship sinking process, supported by experimental validation. Tiago A. Santos and C. Guedes Soares (2008) [14] developed a time-domain model for damaged ships, combined with a shallow-water model to describe the motion of floodwater inside compartments. Gao ZL (2010) [15] proposed a method based on an N–S solver and the VOF method to simulate seawater ingress into a damaged box-shaped structure, with the results compared against model tests. Ypma (2010) [16] developed a numerical tool for simulating damaged ship flooding by coupling compartment flooding with ship motion and verified it through model tests. Gao ZL et al. (2013) [17] combined an N–S solver with a ship seakeeping solver, employing potential flow theory and the VOF method to investigate the roll response of a damaged ship in beam seas. The

simulation results from this integrated approach showed good agreement with experiments. Zhang (2020) [18] adopted and modified the MPS (moving particle semi-implicit) method, applying it to numerically simulate flooding in damaged ship compartments. The study examined flooding through side-shell and bottom breaches, though it was limited to two-dimensional analysis. Valanto P (2022) [19] utilized the HSVA Rolls numerical program to simulate ship flooding after damage, comparing the duration of flooding with and without mitigation measures. Zhang XL (2023) [20] proposed a feasible numerical simulation method to predict the motion response of a damaged DTMB 5415 model in both still water and regular waves. Gao ZL (2024) [21] employed CFD technology to study the motion response of a damaged ship under irregular wave conditions.

#### 1.2.2. Oil Tank Flooding and Leakage

Following the large-scale crude oil spill from the tanker Exxon Valdez, in 1989, new regulations issued by the International Maritime Organization (IMO) (1982) [22] required that new oil tankers must be of double-hull design, either as double-hull tankers (DHTs) or mid-deck tankers (MDTs).

(a) Theoretical research

Sugioka (1999) [23] proposed a model capable of simulating the transformation process of spilled oil, taking into account factors such as current direction, dissolution, diffusion, evaporation, and emulsification. The model computes the distribution and weathering process of spilled oil on the water surface. Tavakoli (2008) [24] applied the Bernoulli differential equation to develop a theoretical model, creating an analytical method for studying oil–water flow through openings in damaged tanks. The model was used to conduct time-domain numerical simulations for various tank designs, validating the effectiveness of double-hull structures in delaying the leakage process and retaining cargo. Goerlandt (2014) [25] introduced a Bayesian network model for estimating oil outflow in ship–ship collisions involving tankers, based on the extent of damage and tank layout to assess the probability of oil leakage. Kollo (2017) [26] developed a hydraulic model to predict the oil outflow from both single-hull and double-hull vessels in collision and grounding scenarios. The model accounts for the influence of breach shape on outflow volume and incorporates subsequent corrections.

(b) Model test

Lin (1994) [27] conducted model test studies on a 1:30 scaled model of a 280,000-ton tanker and a full-scale 40,000-ton double-hull tanker. Numerical simulations were performed and compared with the model test results, verifying the reliability of the numerical approach. Ohtsubo et al. (1994) [28] investigated the failure behavior of tanker structures during collision and grounding through full-scale tests, revealing characteristic failure modes. Katsuji et al. (1996) [29] carried out bottom leakage model tests in still water using a very large crude carrier (VLCC) model tank, examining different loading conditions, scaling ratios, and three types of oil. The study highlighted the importance of satisfying geometric and hydrodynamic similarity criteria in scaled model tests for leakage conditions and cargo properties, though it focused solely on bottom breaches and did not address roll coupling effects induced by side-shell breaches during tank sloshing. Simecek-Beatty (2001) [30] performed a series of leakage model tests on damaged single-hull tanks, investigating the influence of different oil types on leakage characteristics. Tavakoli (2011) [31] employed model testing to study the effects of various tank structural configurations and multiple breach conditions on the oil leakage process, analyzing the role of each factor on instantaneous leakage behavior. Josip Basic (2017) [32] selected appropriate breach locations and sizes, focusing on a tanker with a bottom opening to experimentally and

numerically study its sailing resistance. The results validated that the proposed CFD model and setup could reliably predict the total resistance of the damaged hull and the internal fluid flow in the breached compartment. Lu (2018) [33] conducted model tests and numerical simulations on a very large crude carrier (VLCC) to investigate the coupled motion and leakage mechanisms of a damaged tanker in waves, providing reliable predictions for actual tanker leakage scenarios.

(c) Numerical simulation

Cheng (2010) [34] conducted simulation studies on the oil outflow and stability of a damaged oil tanker using an MPS (moving particle semi-implicit) method-based simulator, accounting for fluid–structure interaction. Tavakoli (2012) [35] employed the CFD software ANSYS Fluent 12.0 to simulate the flooding and leakage of a damaged hull, investigating the effects of fluid density and pressure differential on leakage for different side breach sizes. Yang (2016) [36] utilized a VOF-based multiphase flow solver to simulate the leakage/flooding process of a two-dimensional single-hull oil tank under prescribed periodic motions with varying frequencies and amplitudes. The results indicated that the tank motion not only induces periodic oscillation of the oil–water flow through the breach but also increases the leakage volume during the density-difference-driven stage. Jeong (2016) [37] performed simulations on the motion response of a partially loaded ship in waves, under both intact and damaged conditions, using the PNU-MPS method with a corrected gradient model and a sub-particle-scale turbulence model. Feng (2024) [38] conducted a numerical simulation and analysis of the oil spill phenomenon resulting from leakage after a tanker collision, examining factors such as hull draft, breach size, external current velocity, and oil density, and also investigated the impact of containment measures.

In summary, the model test employed in the study of oil tank leakage are often relatively simplified, with few models selected for double-hull oil-tank structures and limited research on the effects of breach location and size on oil leakage and flooding, and there is a scarcity of experimental research involving oil–water multiphase flow. In contrast, numerical simulations in this area are more abundant, but experimental research in this field is relatively scarce. Therefore, it is essential to conduct model test and numerical simulation studies on the flooding and leakage of damaged double-hull oil tanks in still water.

### *1.3. The Main Research Content of This Paper*

In this study, a model test was conducted to measure a series of physical quantities generated by the flooding and leakage of a damaged double-hull oil tank in still water. Based on a 75,000 DWT oil tanker as the prototype, a scaled tank model was designed for experimental purposes. Following the test plan, measurement data were obtained and corresponding numerical simulations were carried out to analyze the flooding and leakage characteristics of the oil tank under fixed conditions in still water.

## 2. Governing Equations and Numerical Methods

### *2.1. Turbulence Model*

Direct numerical simulation requires immense computational resources. Therefore, to balance time and cost and achieve effective solutions for engineering problems, it is necessary to appropriately simplify the Navier–Stokes equations in the calculations. This paper adopts the RANS model based on the Reynolds-averaged approach.

$$\frac{\partial u_i}{\partial t} + \frac{\partial (u_i u_j)}{\partial x_j} = -\frac{1}{\rho}\frac{\partial p}{\partial x_i} + \frac{\partial (\gamma \cdot 2S_{ij})}{\partial x_j} \quad (1)$$

where $u_i$ and $u_j$ are the velocity components; $t$ represents time; $x_i$ and $x_j$ denote the spatial coordinate components; $\rho$ is the fluid density; $p$ stands for pressure; $\gamma$ indicates the dynamic viscosity coefficient; and $S_{ij}$ corresponds to the components of the strain rate tensor.

In numerical simulations, fully solving the Navier–Stokes (N–S) equations require substantial computational resources. In practice, to improve computational efficiency, turbulence models are often introduced for approximate calculations. Therefore, this study adopts the SST $k$-$\omega$ turbulence model based on the Reynolds-averaged Navier–Stokes (RANS) equations for simulating the flow field.

### 2.2. Volume of Fluid Method

The free-surface capturing method employed in the numerical simulation is the volume of fluid (VOF) method. This method utilizes a fluid volume fraction to describe the distribution of fluid phases and the position of the phase interface, and it tracks the phase interface by solving the transport equation for the phase volume fraction. The governing equation is as follows:

$$\begin{cases} a_i = \frac{V_i}{V} \\ \sum_{i=1}^{N} a_i = 1 \end{cases} \tag{2}$$

$$\frac{\partial a_i}{\partial t} + \nabla(a_i \mathrm{U}) = 0 \tag{3}$$

where $a_i$ is the phase volume fraction; $V$ is the volume of the mesh cell; $V_i$ is the volume of the $i$-th phase within the mesh cell; $N$ is the total number of phases; and U represents the velocity components of phase $i$.

### 2.3. Multi-Region Fluid Phase Distribution

Given the complex fluid distribution involving oil–water–air three-phase flow in the numerical simulation, the field function in the numerical software STAR-CCM+ (Siemens Digital Industries Software, Plano, TX, USA) was applied to configure the computational domain, specify boundary and region values, and define initial conditions. The specific definition of the field function is given by Equation (4).

$$\begin{cases} ((\$\$\mathrm{Position}[0] >= \mathrm{X1})\&\&(\$\$\mathrm{Position}[0] <= \mathrm{X2}) \\ (\$\$\mathrm{Position}[1] >= \mathrm{Y1})\&\&(\$\$\mathrm{Position}[1] <= \mathrm{Y2}) \\ (\$\$\mathrm{Position}[2] >= \mathrm{Z1})\&\&(\$\$\mathrm{Position}[2] <= \mathrm{Z2}))?1:0 \\ \\ ((\$\$\mathrm{Position}[0] >= \mathrm{X1})\&\&(\$\$\mathrm{Position}[0] <= \mathrm{X2}) \\ (\$\$\mathrm{Position}[1] >= \mathrm{Y1})\&\&(\$\$\mathrm{Position}[1] <= \mathrm{Y2}) \\ (\$\$\mathrm{Position}[2] >= \mathrm{Z1})\&\&(\$\$\{\mathrm{Position}\}[2] <= \mathrm{Z2})) \\ ?0 : \$\{\mathrm{VolumeFractionHeavyFluidWave0}\} \end{cases} \tag{4}$$

In the above equation, $$Position [0] represents the X-direction, $$Position [1] represents the Y-direction, $$Position [2] represents the Z-direction, "${VolumeFractionHeavyFluidWave0}" denotes the water volume fraction under the still water VOF wave condition, a value of 1 indicates that the defined region is fully filled with fluid, and a value of 0 indicates that the defined region contains no fluid.

The flow field shown in Figure 1. is divided by the tank walls and the free surface into three regions corresponding to the oil, water, and air phases. A field function is employed to define the initial distribution of the three-phase fluids (oil–water–air) in the flow domain, where green represents oil, red denotes water, and blue indicates air.

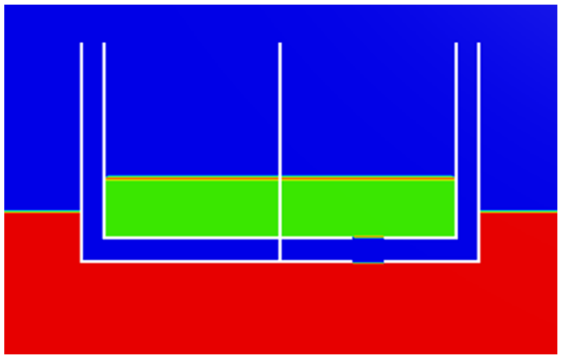


**Figure 1.** Three-phase distribution of oil, water, and gas in the flow filed.

The density of the water phase is 998.5 kg/m$^3$, and the kinematic viscosity is $1.0 \times 10^{-6}$ m$^2$/s. The density of the oil phase is 915 kg/m$^3$, and the kinematic viscosity is $3.2 \times 10^{-5}$ m$^2$/s. The density of the gas phase (air) is 1.225 kg/m$^3$. The surface tension coefficient of water is 0.072 N/m, the surface tension coefficient of oil is 0.023 N/m, and the contact angle is set to 90°.

The specific settings of the boundary conditions and initial conditions in the numerical simulation are shown in Table 1.

**Table 1.** Boundary and initial condition settings.

| Boundary and Initial Condition | Settings |
|---|---|
| Liquid–Solid Interface Condition | $v_{fliud} = v_{wall}$ |
| Liquid–Liquid Interface Condition | $v_1 = v_2$; $p_1 = p_2$ |
| Free Surface Condition | $\tau = 0$; $p = p_{atm}$ |
| Initial Condition | $v(x,y,z,t_0) = v_0(x,y,z)$; $p(x,y,z,t_0) = p_0(x,y,z)$ |

In the above table, $v_{fliud}$ represents the velocity of the fluid motion; $v_{wall}$ represents the velocity of the solid wall; $p$ denotes the pressure; $v$ denotes the velocity; subscripts 1 and 2 correspond to liquid 1 and liquid 2, respectively; $\tau$ represents the shear stress; $p_{atm}$ denotes the atmospheric pressure at the free surface; $v_0$ denotes the initial velocity; and $p_0$ denotes the initial pressure distribution of the flow field.

By employing a user-defined field function, this study achieved precise configuration and distribution of the initial fluid arrangement and physical properties across multiple regions, thereby providing accurate initial conditions and a well-defined physical model for subsequent numerical simulations.

## 3. Experimental Design

### *3.1. Test Facility and Model Design*

The test pool constructed for the model tests measures 3 m × 1.5 m × 1 m (length × width × height), with a water depth of 0.5 m. The prototype of the test model is a 75,000 DWT oil tanker. Following geometric similarity criteria, a scaled model was fabricated at a scale ratio of 1:57.4. The scale ratio satisfies the Reynolds similarity criterion, mainly satisfies the dynamic viscosity and density of the oil, as detailed in Table 2 below. In the model design, emphasis was placed on reproducing key geometric features such as the double-hull structure and the position of the center of buoyancy to ensure that the model's performance resembles that of the prototype ship. Specific dimensions are provided in Table 3.

**Table 2.** Introduction to dimensionless similarity criteria.

| Dimensionless Parameter | Formula | Physical Meaning | Similarity Satisfied in This Model |
|---|---|---|---|
| Froude Number (Fr) | $Fr = \frac{v}{\sqrt{gL}}$ | Ratio of inertial forces to gravitational forces | Deviation within acceptable range (governs gravity-driven flows, such as the oil discharge velocity at the breach) |
| Reynolds Number (Re) | $Re = \frac{\rho v L}{\mu}$ | Ratio of inertial forces to viscous forces | Satisfied the kinematic viscosity and density of the oil (turbulent mixing and oil dispersion during the leakage process) |
| Weber Number (We) | $We = \frac{\rho v^2 L}{\sigma}$ | Ratio of inertial forces to surface tension forces | Not satisfied (at small scales or for small breach sizes, surface tension can influence film rupture and droplet formation; negligible at large scales) |

**Table 3.** Main dimensions and parameters of the hull.

| Parameter | Symbol | Value | Unit |
|---|---|---|---|
| Length Overall | $L_{OA}$ | 228 | m |
| Length Between Perpendiculars | $L_{PP}$ | 224 | m |
| Breadth | $B$ | 36 | m |
| Depth | $D$ | 20 | m |
| Draft | $T$ | 12.2 | m |
| Displacement | $\Delta$ | 90,100 | t |
| Vertical Center of Gravity | $KG$ | 11.73 | m |
| Longitudinal Center of Gravity | $LCG$ | 114.626 | m |
| Deadweight | $DWT$ | 75,000 | t |
| Capacity | $V$ | 88,000 | $m^3$ |

The liquid tank model is a six-compartment, open-top double-hull oil tank. This design is a simplified representation of an actual oil tanker's compartment layout, intended to focus on investigating the core characteristics of liquid sloshing and flooding/leakage while avoiding interference from complex structural members (such as trusses and floors) present in real-world compartments. It comprises two central liquid cargo tanks and two ballast tanks. The total mass of the model is 11.97 kg. The model's structure and its coordinate system are illustrated in Figure 2.

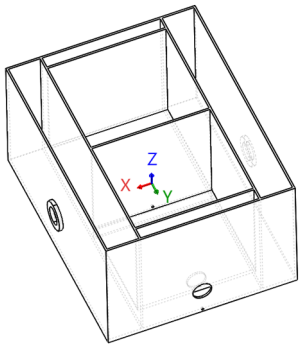



**Figure 2.** Schematic diagram of the oil tank model and its coordinate axes.

Both oil tanks are filled with vegetable oil with a density of approximately 915 kg/$m^3$, which is dyed red using an oil-soluble coloring agent for visual observation. The breach on the tanks were sealed with plugs, which are rapidly removed by pulling attached thin threads to simulate the damage. This method introduces minimal interference to the tank motion and the free liquid surface, and its effect is considered negligible. The same plug-sealing method is also used to ensure the watertight integrity of the tanks. The tanks are left stationary in water

for 3 h, and the absence of flooding into the ballast tanks confirms the watertight reliability of this sealing approach. For different breach sizes, corresponding plugs are custom-made to match each breach. Detailed schematics of the plugs are provided in Figure 3.



**Figure 3.** Schematic diagram of water-tight rubber stoppers.

The specific dimensions of the model are shown in Figure 4 below. The oil tank model was positioned at the center of the test pool, with a support frame system installed above it to connect displacement-restriction devices (As shown in Figure 5). The displacement-restriction device, mounted on the I-beams, serves to secure the oil tank in a fixed position. Due to their high strength, I-beams experience negligible deformation or fracture under load, effectively preventing vertical displacement of the chrome-plated guide shafts caused by the self-weight of the support frame or external loads, thereby reducing error in model tests. For this purpose, two I-beams, each 2 m in length, were employed as crossbeams spanning over the test pool to serve as the primary support structure.

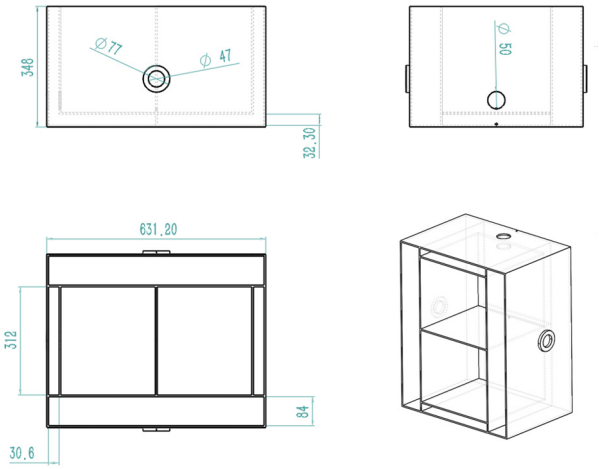



**Figure 4.** Three-view drawings of the test model.

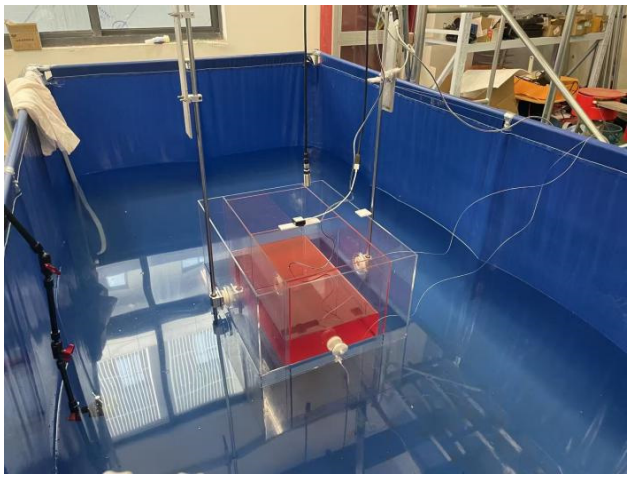


**Figure 5.** Assembly diagram of the oil tank model.

### 3.2. Experimental Measurement System and Test Conditions

Pulsating Pressure Sensor (Nanjing Youlide Scientific Instrument Co., Ltd. Nanjing, China): Model CY302, with a measurement range of 0~10 kPa, an output voltage of 12~24 V, a dynamic frequency of 10 KHz, and an accuracy of 0.10% FS. The pulsating pressure sensor is illustrated in Figure 6. The arrangement of pressure monitoring points is shown in Figure 7.



**Figure 6.** Schematic diagram of the equipment.

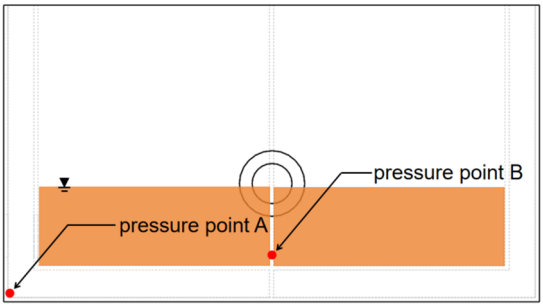



**Figure 7.** Schematic diagram of pressure measurement point.

The shape and dimensions of side-shell breaches in ships are primarily influenced by factors such as the size and geometry of the bulbous bow during collision, the impact angle, and the kinetic energy carried by the vessel. Bottom openings, on the other hand, are mostly caused by grounding accidents and are largely affected by various seabed features (such as rocks, reefs, and shoals). Such breaches often exhibit irregular diamond or irregular circular shapes. In this study, the test condition settings are set as shown in Table 4. To facilitate the experiment, an idealized circular shape is adopted for the breach openings (specific breach configurations are listed in Table 5).

**Table 4.** Test condition settings.

| Breach Location | Case | Breach Size (Diameter) |
|---|---|---|
| Side-shell | C1 | 5 cm |
| | C2 | 3.75 cm |
| | C3 | 2.5 cm |
| Bottom | G1 | 5 cm |
| | G2 | 3.75 cm |
| | G3 | 2.5 cm |

**Table 5.** Settings of perforation conditions.

| Breach Location | Breach Shape | Breach Size |
|---|---|---|
| Side, Bottom | Circular | 2.5 cm, 3.75 cm, 5.0 cm |

According to maritime accident reports compiled by EMSA (2021) [1], incidents of tanker damage caused by collisions and groundings account for more than 50% of all cases. Additionally, based on Lloyd's Register global shipping accident statistics, a total of 3976 total loss incidents involving vessels of 100 gross tons and above were recorded worldwide between 1998 and July 2018. The data indicate that hull breaches are predominantly located in the midship section, with breach dimensions generally ranging from approximately 2 to 4 m relative to the ship's scale. Circular breaches were selected for this experiment. Based on a scale factor of 1:57.4, the breach diameters were set to 2.5 cm, 3.75 cm, and 5 cm, respectively.

During the model test, underwater and external motion cameras recorded the process simultaneously. Once the sensors began data acquisition, the plug was withdrawn to trigger tank flooding/leakage. Data recording was terminated after the tank model ceased leaking and internal liquid exchange reached a steady state. Data from the moment of breach initiation until liquid exchange stopped were selected to generate time-history curves of motion response and pressure. The experimental results presented in the figures and tables correspond to a single test trial. The results of this model test are in good agreement with the numerical simulation.

## 4. Numerical Setup

### *4.1. Computational Domain*

Within the computational domain, the following two primary regions are defined: the background region and the oil tank region, as shown in Figure 8. The background region is used to simulate the test pool, maintaining the same dimensions as the test pool. Its upper boundary is set as a pressure outlet, while all other boundaries are designated as wall surface. The oil tank model is also configured as a wall surface.

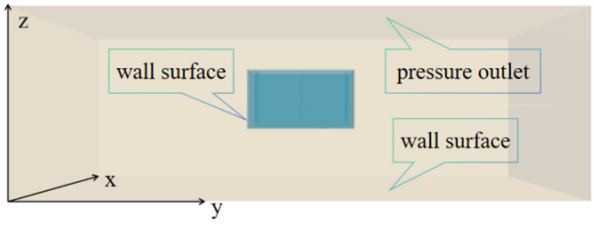



**Figure 8.** CFD simulation domain for oil tank leakage.

### *4.2. Mesh Generation and Solver Settings*

In the CFD simulation, a trimmed mesh is employed to generate the grid for the computational domain, as shown in Figure 9. During meshing, appropriate local refinement is applied to regions with significant flow variations, such as around the breach opening of the oil tank, the surrounding flow field near the tank model, and the free surface area.

The minimum mesh size in the background region is 0.01 m. The mesh in the overset region must satisfy a size ratio no greater than 1:2 relative to the background mesh. Accordingly, the mesh size in the free surface zone within the overset region is set to 0.08 m, and the refined zone around the breach is set to 0.005 m, all of which meet the convergence study requirements.

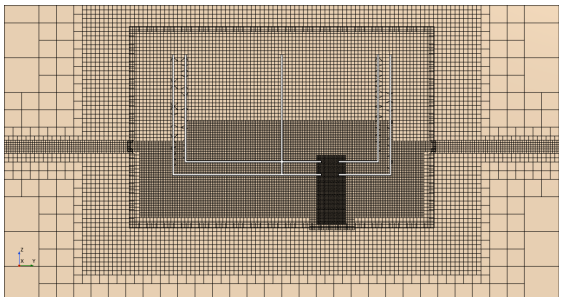


**Figure 9.** The distribution of the computational domain grid.

In the CFD solver settings, the multiphase flow simulation employs the volume of fluid (VOF) method. The free surface is initialized as a still water VOF wave, and the turbulence model is set to the SST $k$-$\omega$ model. To ensure computational accuracy and enable comparison with model tests, the Courant number is maintained below 1. The time step for the CFD simulation is set to 0.001 s, with 10 iterations per step.

### *4.3. Numerical Simulation Validation*

1. Time step validation

Prior to conducting numerical simulations, validation of the numerical software is required. Taking the case with a bottom breach diameter of 5 cm as an example, three different time steps (0.005 s, 0.001 s, and 0.0005 s, the iteration count is set to 10) were set for comparative validation against experimental results. As can be seen from Figure 10 below, there is a certain degree of pressure error during the oil leakage process, but the comparison results are in good agreement. Moreover, it can effectively capture the peak slamming pressure generated at the moment of tank breach.

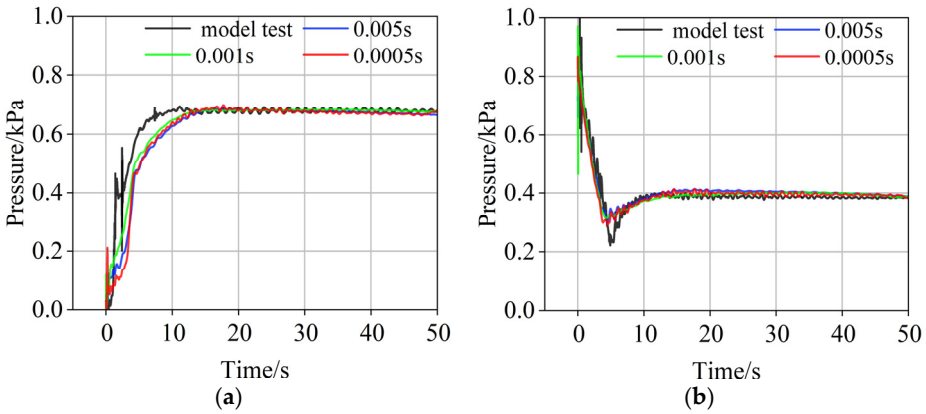



**Figure 10.** Comparison of pressure time histories for different time steps: (**a**) pressure point A; (**b**) pressure point B.

2. Mesh validation

To verify mesh independence, three mesh configurations—coarse, medium, and fine—were generated, with the mesh size and total cell count progressively refined by a factor of approximately 1.41 between successive levels, as shown in Table 6. The free surface, the area around the oil tank, and the breach area were refined with a finer mesh. The computational results obtained from these three meshes were then compared against experimental data. As can be seen from Figure 11 below, the simulation results obtained with the three different mesh resolutions all show good agreement with the experimental values. Comparatively, the medium mesh yields the best agreement.

**Table 6.** Mesh spacing configuration for mesh independence verification.

| Mesh Spacing | Minimum Cell Size | Total Number of Cells |
|---|---|---|
| Fine | 0.008 m | 3,816,000 |
| Medium | 0.01 m | 2,612,000 |
| Coarse | 0.013 m | 1,882,000 |

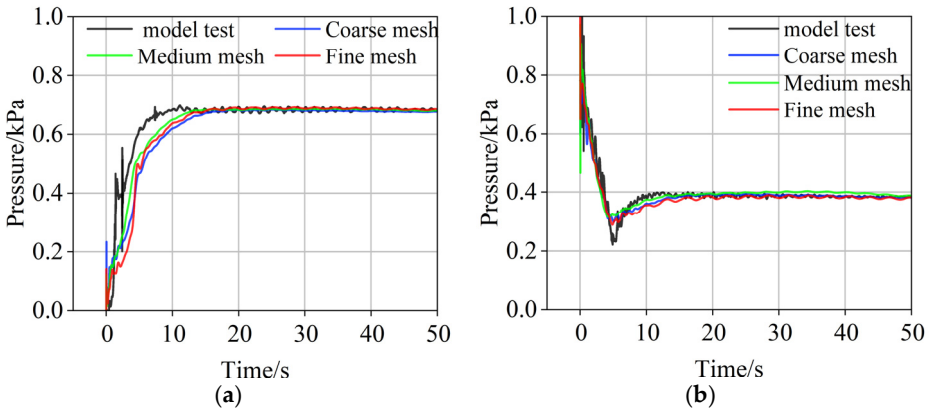



**Figure 11.** Comparison of pressure time histories for different mesh resolutions: (**a**) pressure point A; (**b**) pressure point B.

## 5. Results and Discussion

### *5.1. Side-Shell Damage*

1. Model test

For the three breach sizes of different diameters, the pressure variations over time at pressure points A and B were measured respectively (as shown in Figure 12). Figure 12c indicates that during the initial stage of leakage, the discharge of oil from the tank and the flooding are primarily driven by the pressure differential between the interior and exterior, as well as gravity. The oil leakage rate is relatively high, and the liquid level drops rapidly, then gradually slows down and stabilizes. By comparing the pressure curves of the breach diameter—C1 (5 cm), C2 (3.75 cm), and C3 (2.5 cm)—in the figure, it can be observed that C1, C2, and C3 reached stable pressure at 7.30 s, 9.40 s, and 14.10 s, respectively. This demonstrates that a larger breach diameter leads to faster leakage and quicker pressure stabilization. Particularly at the moment of breach opening, the leakage process is accompanied by a pronounced slamming phenomenon. Furthermore, it can be observed that the smaller the breach size, the longer the leakage duration and the sloshing time inside the tank, and the greater the pressure fluctuation. As shown in Figure 12d, the pressure curves for C1, C2, and C3 are relatively smoother but stabilize at approximately 7.30 s, 9.90 sand 15.50 s, respectively. From the captured photographs in Figure 12 (using case C1 as an example, where the green line indicates the oil water interface and the extent of oil dispersion), it can be further observed in image (4) that at t = 4.00 s, the oil rapidly gushes out in a jet like flow. Part of the oil is intercepted by the ballast tank, while the remainder leaks directly into the external water body, spreading quickly and accompanied by vortex formation. This is because the model more closely resembles a real double-hull tanker structure. During the pressure difference driven leakage phase, the leakage of oil and the flooding mutually impact each other, which traps a portion of the oil inside the ballast tank, dissipates its kinetic energy, and leads to a certain degree of oil sealing effect, thereby suppressing further oil leakage. Meanwhile, due to scale effects, the viscous force of the oil has a certain influence, particularly on the leakage rate and the oil–water mixing pattern during the exchange between water and oil.

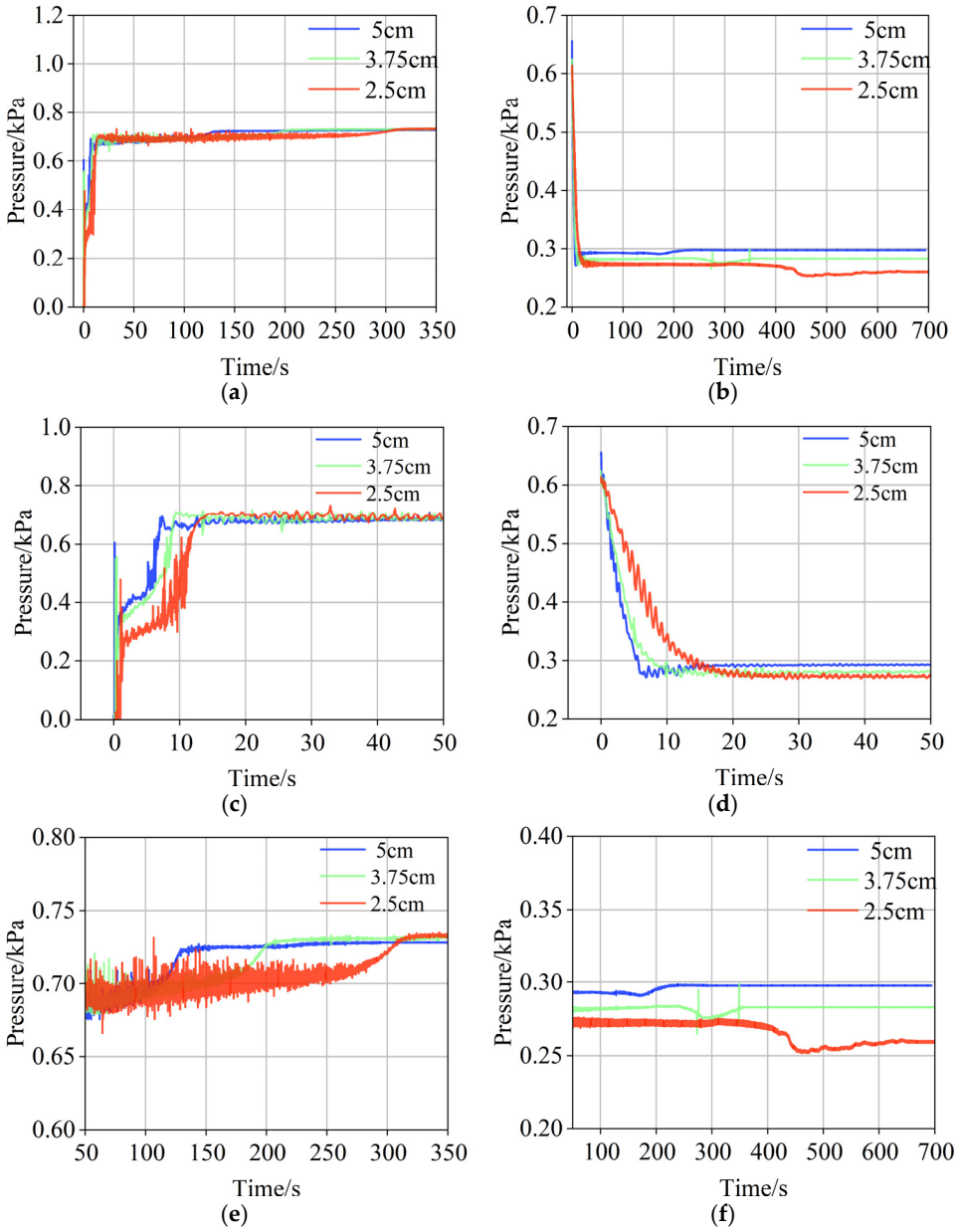



**Figure 12.** Pressure time history plots of pressure points A and B for C1, C2, and C3: (**a**) pressure point A (0~350 s); (**b**) pressure point B (0~700 s); (**c**) pressure point A (0~50 s); (**d**) pressure point B (0~50 s); (**e**) pressure point A (50~350 s); (**f**) pressure point B (50~700 s).

As shown in Figure 12e, in the later stage of the leakage process, the outflow of oil from the tank is primarily driven by the density difference between the oil and the external water, and the leakage rate significantly decreases. In the figure, case C1, C2, and C3 successively reach a stable state, demonstrating that a larger breach diameter leads to faster leakage, earlier stabilization, and sooner cessation of leakage in this phase. As captured in the underwater photographs of Figure 13 (2) and (3), during the density-difference-driven leakage phase, although the oil tank and ballast tank are filled with intercepted oil, the lower density of oil compared to water leads to a slow displacement process between oil and water. This gradually expels the oil from the tank, ultimately leaving the interior occupied mainly by water with only a small amount of residual oil. Based on the above analysis and existing related research, it can be concluded that the leakage process from a side-shell breach of an oil tank mainly consists

of the following two distinct stages: the pressure-difference-driven leakage stage and the density-difference-driven leakage stage.

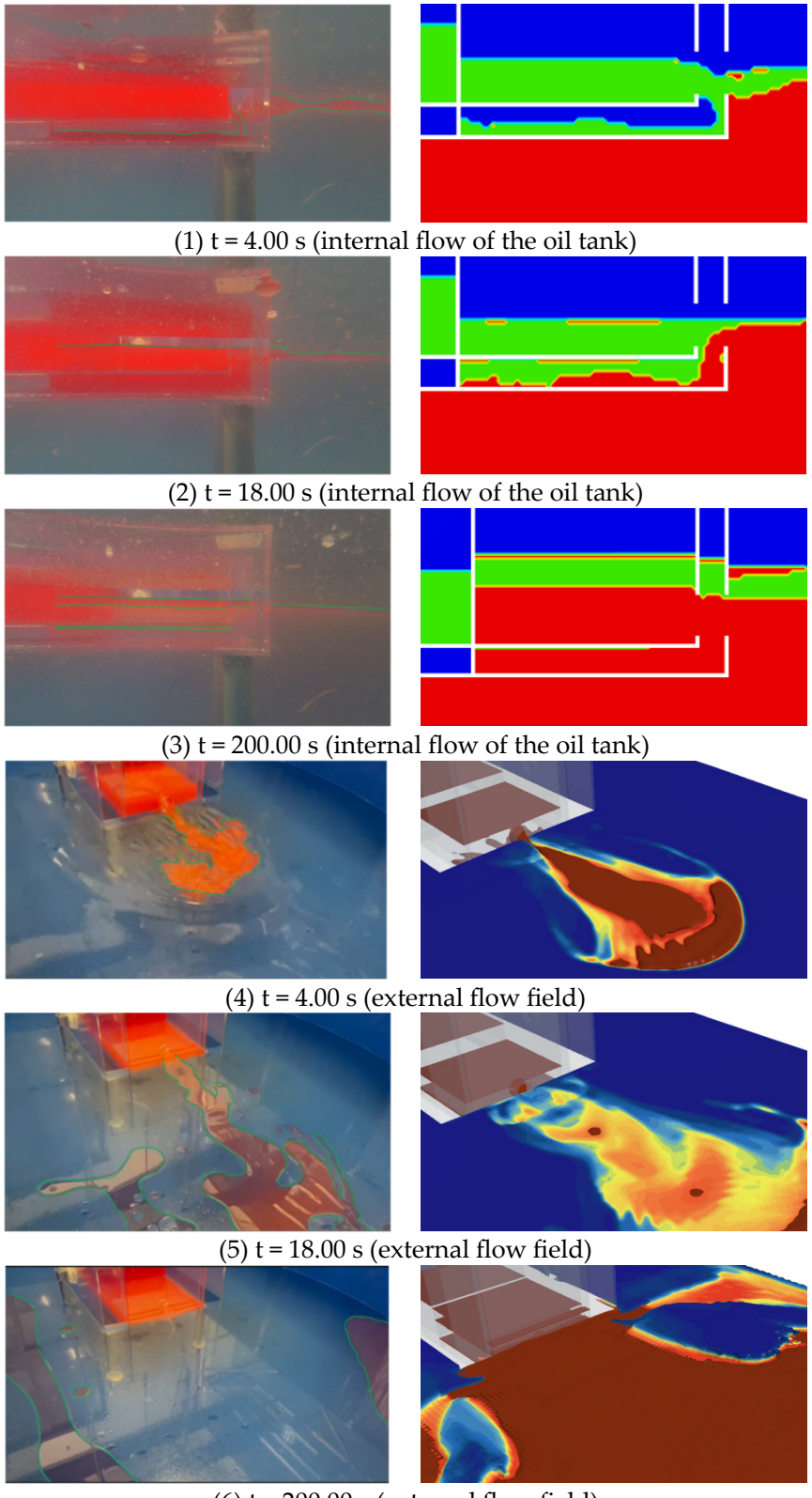



**Figure 13.** Comparison diagram of flow field and free surface from model test and numerical simulation under fixed-state side-shell breach conditions. (The oil phase is shown in red, the water phase in blue).

As shown in Figure 12d,f, pressure point B is located in the upper oil tank, and its pressure trend exhibits an opposite pattern compared to that at point A in the lower part of the ballast tank. Point B reflects the internal pressure variation of the oil tank, and its pressure changes more gradually than those recorded at point A in the ballast tank. Furthermore, due to the different breach sizes, the opening in case C3 remains submerged, whereas those in cases C2 and C1 are partially exposed above the water surface. Because of the density difference between oil and water, a small amount of oil is retained above the opening in case C3. Consequently, the stabilized pressures under the three cases differ to some extent due to the varying degrees of oil retention.

## 2. Numerical simulation

This section focuses on the post-processing of numerical simulation results and their comparison with the pressure time-history curves captured during the model tests. Additionally, the flow field images and liquid surface photographs obtained from the model tests are compared with the numerical simulation results, followed by an analysis of the sources of discrepancy.

As shown in Figure 14a,c,e, the pressure in the numerical simulation stabilizes at 6.17 s, 8.67 s, and 12.21 s, respectively. Compared with the model test results, the pressure errors at monitoring point A for cases C1, C2, and C3 are 7.5%, 7.9%, and 13.8%, respectively. And in Figure 14b,d,f, the pressure in the numerical simulation stabilizes at8.03 s, 13.21 s, and 22.95 s, respectively. The pressure errors at monitoring point A for cases C1, C2, and C3 are 5.1%, 5.2%, and 8.7%, respectively. It can be concluded that the employed CFD software is capable of reasonably simulating the pressure during tank leakage/flooding, with results that generally align with the model test data. However, the numerical simulation shows a slower stabilization of pressure during the leakage process compared to the model test. Furthermore, the simulation software cannot capture the slamming effect generated during tank leakage as sensitively as pressure sensors, nor can it fully reproduce the pressure fluctuations that occur throughout the leakage process. Of course, the numerical simulation software offers greater stability and can eliminate the effects caused by design flaws in the experimental setup, such as disturbances introduced during the creation of the tank breach. Additionally, by comparing with Figure 13, the internal scenario of the oil tank in the numerical simulation similarly shows that oil is leaked first, followed by the filling of the ballast tank, along with a small amount of flooding, and a gradual displacement process occurs. In the external still-water environment, the oil in the numerical simulation also leaks into the external environment in a jet-like pattern, forming an oil slick on the water surface. However, compared with the actual model test, no pronounced vortices are generated in the simulation. This is primarily due to the use of the SST k-ω turbulence model, which still exhibits certain discrepancies from physical reality. Ultimately, when the flooding and leakage inside the oil tank cease, the model test shows that only water and a thin residual layer of oil remain in the tank and ballast compartments. A similar distribution is observed in the numerical simulation. Meanwhile, once the external flow field stabilizes at t = 200.00 s, a large amount of oil has spread and covered the free surface, forming an extensive oil slick.

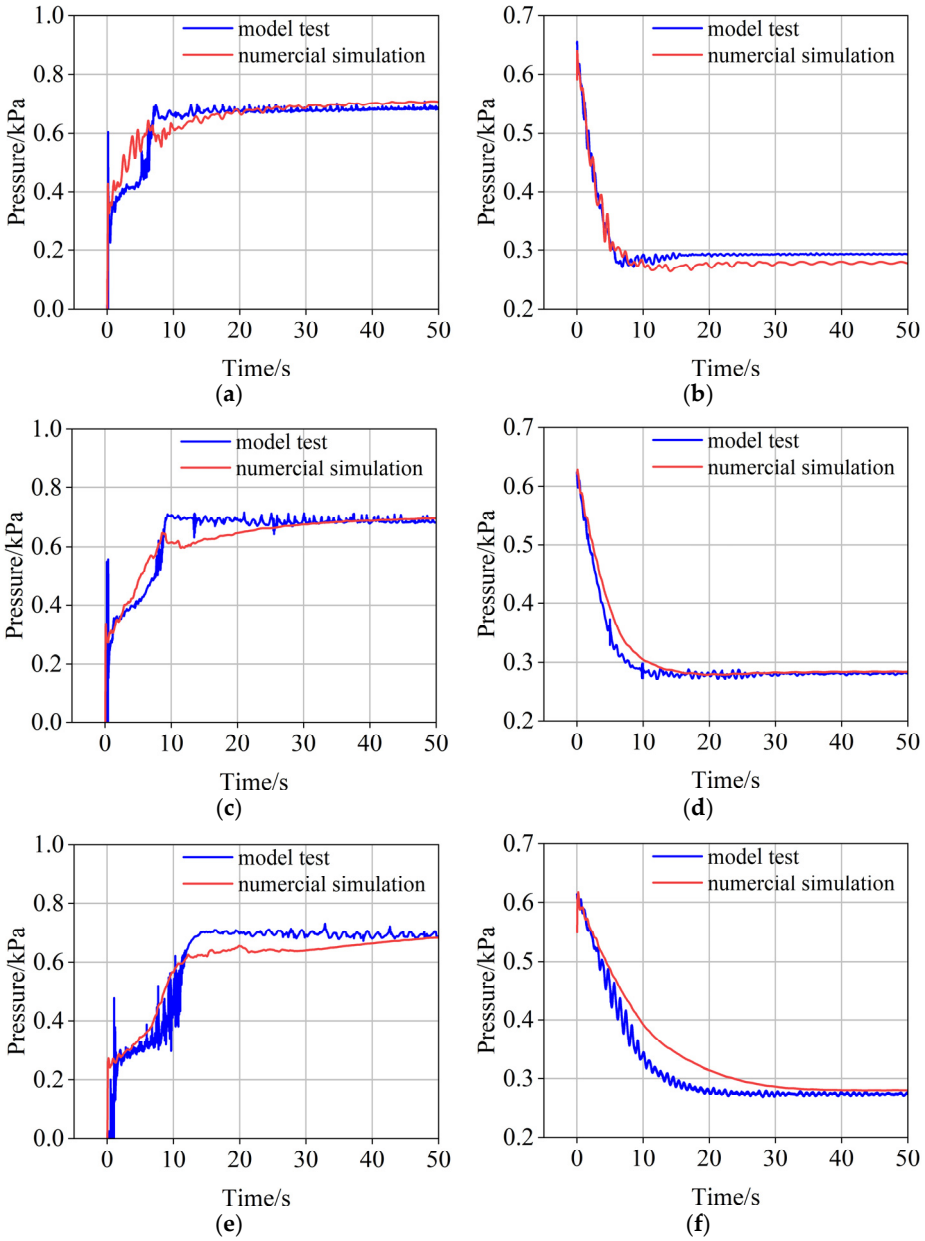



**Figure 14.** Comparison plot of pressure between model tests and numerical simulations for C1, C2, and C3: (**a**) pressure point A (C1); (**b**) pressure point B (C1); (**c**) pressure point A (C2); (**d**) pressure point B (C2); (**e**) pressure point A (C3); (**f**) pressure point B (C3).

### *5.2. Bottom Damage*

1. Model test

Under the condition of a bottom breach in the oil tank model, Figure 15a,b indicate that the bottom breach is influenced solely by gravity, with no density-difference-driven leakage stage. At the instant the bottom breach occurs, the oil rapidly leaks downward due to its substantial potential energy. Part of the oil discharges into the external water pool, while another portion is intercepted in the lower section of the ballast tank; simultaneously, a small amount of external water enters the tank. Because the density of oil is lower than that of water, the water entering the ballast tank through the bottom breach does not continue to leak out due to density differences. Instead, an oil-sealing phenomenon occurs: the water firmly traps the oil inside the tank, leading to a faster stabilization compared to the side-shell breach case. Furthermore, as shown in Figure 15a, the pressure stabilized at

approximately 7.70 s, 10.50 s, and 24.60 s for cases G1, G2, and G3, respectively, whereas in Figure 15b stabilization occurred at about 8.40 s, 11.70 s, and 25.60 s. Since the ballast tank is located below the oil tank, it is the first to experience flooding and oil leakage and is less prone to sloshing. Therefore, the pressure in the ballast tank stabilizes earlier than that at the pressure point B in the oil tank.

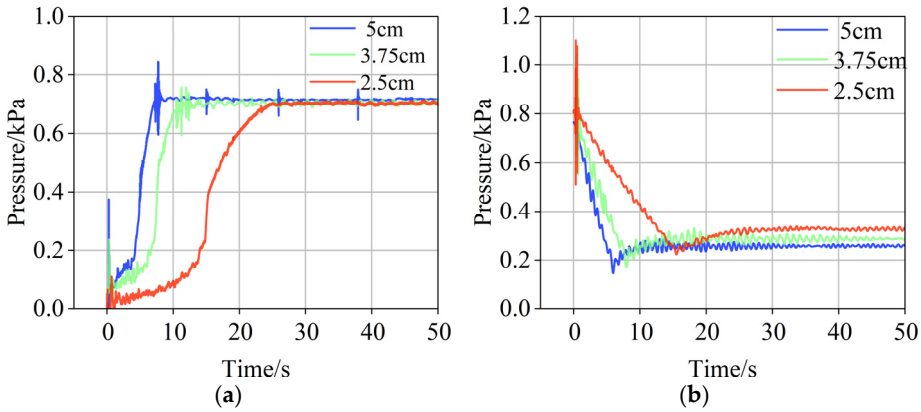



**Figure 15.** Pressure time history plots of pressure points A and B for G1, G2, and G3: (**a**) pressure point A (0~50 s); (**b**) pressure point B (0~50 s).

Similar to the side-shell breach condition, a slamming phenomenon also occurs at the moment when the bottom breach is opened, and this dynamic response is effectively captured by both monitoring points. Furthermore, as shown in Figure 15a,b, the stabilization times for cases G1 (5 cm), G2 (3.75 cm), and G3 (2.5 cm) decrease successively. This indicates that a larger breach diameter results in a higher leakage rate, a shorter stabilization time, and the extent of flooding into the ballast tank also increases accordingly. This trend is reflected consistently in the pressure variations observed in both the ballast tank and the oil tank.

Combined with the results shown in Figure 16 (taking case G3 as an example), the above conclusions can be further substantiated. During the bottom leakage process, a limited amount of water also enters the oil tank. This is primarily due to the instantaneous pressure differential created, which drives a small volume of flooding into the tank, resulting in restricted exchange with the oil inside. Although this leads to partial flooding of the oil tank, its impact on the overall leakage behavior remains relatively minor.

2. Numerical simulation

The pressure curves for the bottom-breach cases (G1, G2, and G3) in the numerical simulation generally align well. As shown in Figure 17a,c,e, the pressure in the numerical simulation stabilizes at 7.67 s, 10.73 s, and 27.46 s, respectively. Compared with the model test results, the pressure errors at monitoring point A for cases G1, G2, and G3 are 2.7%, 5.6%, and 5.4%, respectively. And in Figure 17b,d,f, the pressure in the numerical simulation stabilizes at 9.34 s, 12.71 s, and 27.07 s, respectively. The pressure errors at monitoring point A for cases G1, G2, and G3 are 1.3%, 6.7%, and 3.0%, respectively. It can be concluded that the employed CFD software is capable of reasonably simulating the pressure during tank leakage/flooding, with results that generally align with the model test data. However, the comparison of curves from pressure points A and B reveals that the leakage stabilizes more rapidly in the simulation, with fewer fluctuations relative to the model tests. Furthermore, when comparing the scenario captured in the numerical simulation (Figure 16), it shows that the leaking oil impacts the water inside the tank, forming an oil column. In the simulation, the discharged oil rises more quickly and is intercepted by the ballast tank. Nevertheless, by t = 50.00 s, the oil level inside the ballast tank in the simulation is lower

than that in the actual test, indicating that a smaller amount of oil is retained compared with the physical model test. Consequently, the pressure monitored in the oil tank is also lower than in the experiment. Additionally, regarding the spreading of oil on the free surface in the external flow field, the model test shows that after leakage the oil not only forms an oil slick but also breaks into fine droplets that disperse on the free surface and are difficult to capture. In the numerical simulation, the area of oil spreading is larger, and, similarly, some oil adheres to the side of the model.

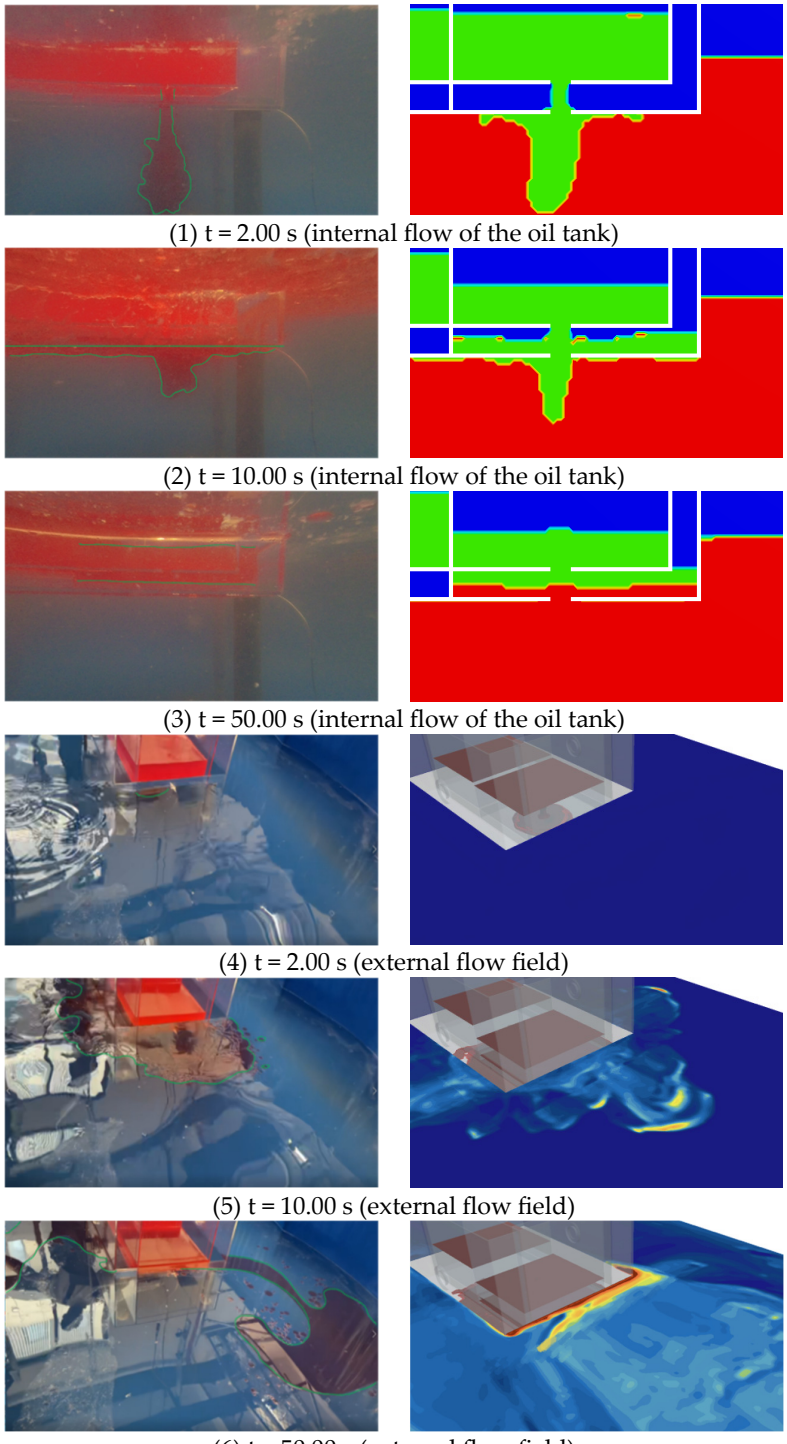



**Figure 16.** Comparison diagram of flow field and free surface from model test and numerical simulation under fixed-state bottom damage conditions. (The oil phase is shown in red, the water phase in blue).

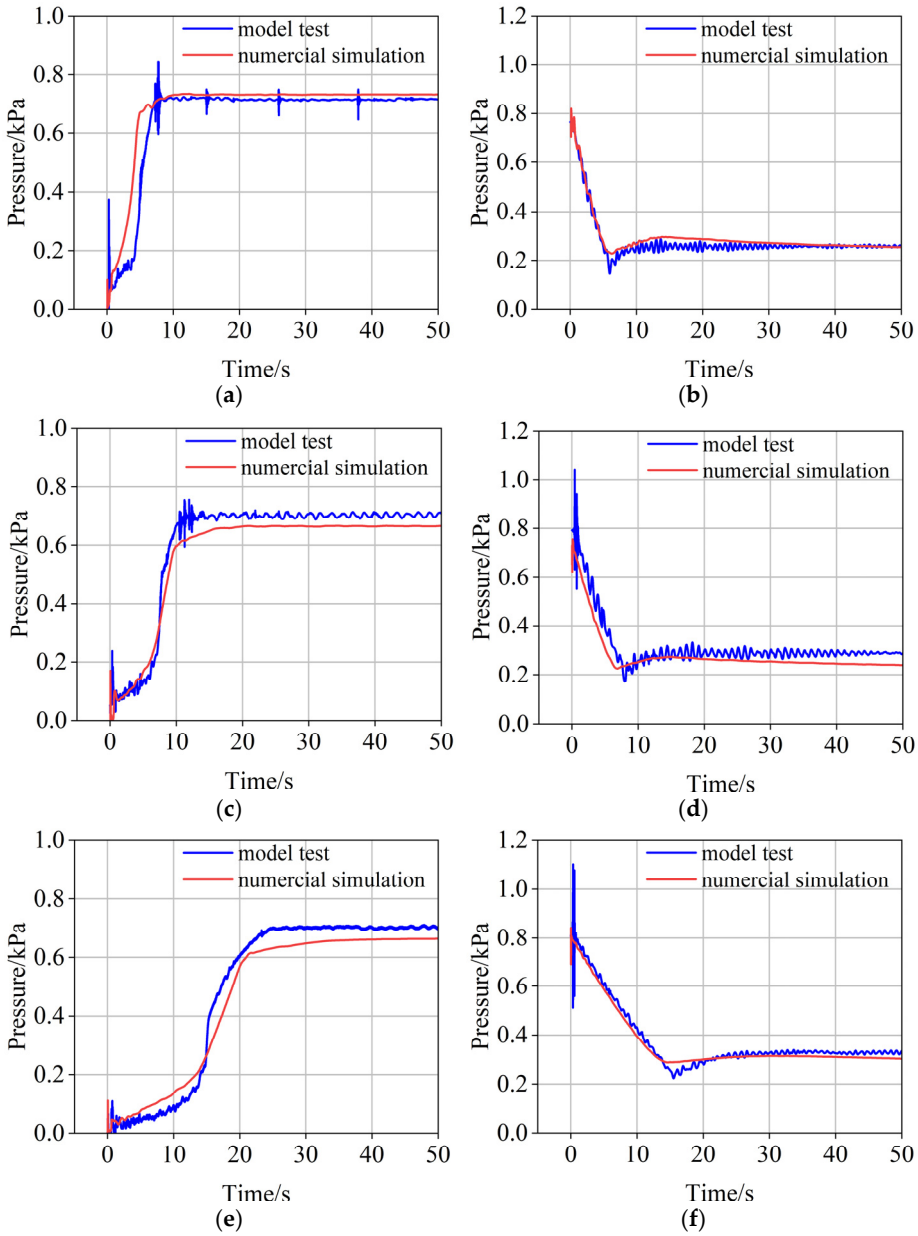



**Figure 17.** Comparison plot of pressure between model tests and numerical simulations for G1, G2, and G3: (**a**) pressure point A (G1); (**b**) pressure point B (G1); (**c**) pressure point A (G2); (**d**) pressure point B (G2); (**e**) pressure point A (G3); (**f**) pressure point B (G3).

### *5.3. Error Analysis*

(1) Manufacturing tolerances of the oil tank model: These mainly arise from limitations in material properties and fabrication techniques. The model was manually constructed using transparent acrylic sheets. Due to precision constraints during the cutting and bonding process, a tolerance of approximately 1 mm exists. Furthermore, during the casting of the acrylic sheets, uneven heat dissipation causes the edges to solidify before the central part, resulting in a non-uniform thickness distribution where the edges are thicker than the middle. During manual assembly, it is challenging to ensure that all panels are perfectly vertical or horizontal, introducing additional assembly deviations. Collectively, these factors lead to discrepancies in physical parameters such as the dimensions, center of gravity, and moment of inertia between the fabricated oil tank model and its theoretical counterpart in numerical simulation software.

(2) Synchronization errors: the operational process may lead to a certain deviation between the actual start time of data acquisition and the initial time set in the numerical simulation.
(3) Instrumentation errors: Pressure sensors are primarily suited for monitoring single-phase water media. When applied to multiphase flows, particularly those involving oil, the measured pressure values can vary due to differences in the physical properties of oil and water phases. Additionally, after prolonged use, oil residues are difficult to remove completely, which may cause minor drift errors in the sensors. The angle sensor is mounted on the surface of the oil tank model and requires zeroing before each test. However, the instrument itself exhibits inherent amplitude fluctuations of approximately $\pm 0.01^{\circ}$, which also introduces a certain level of measurement error.

## 6. Conclusions

Through the experimental and numerical study and analysis of leakage characteristics in a damaged double-hull oil tank in a fixed state, the following conclusions are drawn:

(1) The larger the breach diameter, the faster the leakage rate and the shorter the time required for stabilization. For side-shell breaches case, pressure stabilized at approximately 7.30 s, 9.40 s, and 14.10 s for cases C1, C2, and C3, respectively. For bottom breaches case, pressure stabilized at about 7.70 s, 10.50 s, and 24.60 s for cases G1, G2, and G3, respectively.
(2) Leakage from a side-shell breach can be divided into a pressure-difference-driven stage and a density-difference-driven stage. In contrast, leakage from a bottom breach is influenced solely by gravity. Moreover, the amount of oil leaked from a bottom breach is affected by the breach diameter—larger diameters result in greater leakage.
(3) The pressure time-history curves monitored in the numerical simulation and the images of tank leakage captured agree well with the model tests. However, the numerical simulation still has limitations in pressure monitoring and scenario representation compared with the physical experiments.

The double-hull structure can retain a portion of the oil, and its performance in containing water-sealed oil leakage after damage is superior to that of a single-hull tank. This has significant engineering implications for mitigating oil spillage during emergency response.

**Author Contributions:** Conceptualization, W.Z.; methodology, W.Z.; software, W.Z.; validation, W.Z.; formal analysis, W.Z.; investigation, W.Z., Q.Q. and H.Z.; resources, R.Z.; data curation, W.Z.; writing—original draft preparation, W.Z.; writing—review and editing, W.Z.; visualization, W.Z.; supervision, X.Z.; project administration, R.Z. and X.Z.; funding acquisition, R.Z. All authors have read and agreed to the published version of the manuscript.

**Funding:** This research was funded by the Natural Science Foundation of Jiangsu Province grant number [BK20241016] and the APC was funded by National Natural Science Foundation of China [52271318].

**Data Availability Statement:** The data presented in this study are available on request from the corresponding author due to privacy.

**Conflicts of Interest:** The authors declare no conflict of interest.

## References

1. EMSA. *Annual Overview of Marine Casualties and Incidents*; European Maritime Safety Report; European Maritime Safety Agency: Lisbon, Portugal, 2022.
2. Zaraphonitis, G.; Papanikolaou, A.; Spanos, D. On a 3-D mathematical model of the damage stability of ships in waves. In Proceedings of the 6th International Conference on Stability of Ships and Ocean Vehicles, Varna, Bulgaria, 22–27 September 1997; Volume 1, pp. 81–98.

3. Fthenakis, V.M.; Rohatgi, U.S. A model of liquid releases from a submerged vessel. *J. Loss Prev. Process Ind.* **1999**, *12*, 437–449. [CrossRef]
4. Santos, T.A.; Winkle, I.E.; Soares, C.G. Time domain modelling of the transient asymmetric flooding of ro–ro ships. *Ocean. Eng.* **2002**, *29*, 667–688. [CrossRef]
5. Zhang, A.M.; Cao, X.Y.; Ming, F.R.; Zhang, Z.F. Investigation on a damaged ship model sinking into water based on three dimensional SPH method. *Appl. Ocean. Res.* **2013**, *42*, 24–31. [CrossRef]
6. Siddiqui, M.; Greco, M.; Lugni, C.; Faltinsen, O. Experimental studies of a damaged ship section in beam sea waves. *Appl. Ocean. Res.* **2020**, *97*, 102090. [CrossRef]
7. Liu, W.B.; Ming, F.R.; Chen, H.; Zhang, A. Experimental study on the air cushion effect during the flooding process of a damaged ship cabin. *Phys. Fluids* **2023**, *35*, 082114. [CrossRef]
8. Papanikolaou, A.; Zaraphonitis, G.; Spanos, D.; Boulougouris, E. Investigation into the capsizing of damaged ro-ro passenger ships in waves. In Proceedings of the 7th International Conference on Stability for Ships and Ocean Vehicles, STAB2000, Launceston, Australia, 7–12 February 2000; pp. 1–12.
9. Jasionowski, A. An Integrated Approach to Damage Ship Survivability Assessment. Ph.D. Thesis, University of Strathclyde, Glasgow, UK, 2001; pp. 9–164.
10. Gao, Q. CFD simulation of water ingress into damaged ships. *J. Ship Mech.* **2001**, *5*, 8–17.
11. Fujiwara, T.; Haraguchi, T. Roll motion of ro-ro passenger ship with flooded vehicle deck. *Int. J. Offshore Polar Eng.* **2005**, *15*, 109–116.
12. Ruponen, P. Progressive Flooding of a Damaged Passenger Ship. Master's Thesis, Helsinki University of Technology, Helsinki, Finland, 2007; pp. 15–114.
13. Valanto, P. *Research Study on the Sinking Sequence and Evacuation of the MV Estonia—Final Report*; Technical Report 1663; HSVA: Hamburg, Germany, 2008; pp. 10–20.
14. Santos, T.A.; Soares, C.G. Study of damaged ship motions taking into account floodwater dynamics. *J. Mar. Sci. Technol.* **2008**, *13*, 291–307. [CrossRef]
15. Gao, Z.; Vassalos, D.; Gao, Q. Numerical simulation of water flooding into a damaged vessel's compartment by the volume of fluid method. *Ocean. Eng.* **2010**, *37*, 1428–1442. [CrossRef]
16. Ypma, E.L.; Turner, T. An approach to the validation of ship flooding simulation models. In Proceedings of the 11th International Ship Stability Workshop, Wageningen, The Netherlands, 21–23 June 2010; pp. 1–12.
17. Gao, Z.; Gao, Q.; Vassalos, D. Numerical study of damaged ship flooding in beam seas. *Ocean. Eng.* **2013**, *61*, 77–87. [CrossRef]
18. Zhang, G.; Wu, J.; Sun, Z.; el Moctar, O.; Zong, Z. Numerically simulated flooding of a freely-floating two-dimensional damaged ship section using an improved MPS method. *Appl. Ocean. Res.* **2020**, *101*, 102207. [CrossRef]
19. Valanto, P. Active Flooding Mitigation for Stability Enhancement in a Damaged RoPax Ship. *J. Mar. Sci. Eng.* **2022**, *10*, 797. [CrossRef]
20. Zhang, X.L.; Li, P.; Mancini, S. Numerical investigation into motion responses of the intact and damaged DTMB 5415 based on the AMR method in regular waves. *Ships Offshore Struct.* **2023**, *18*, 721–734. [CrossRef]
21. Gao, Z.; Shi, Z. Numerical study on damaged ship rolling and capsizing in irregular beam waves during quasi-steady flooding. *Ocean. Eng.* **2023**, *289*, 11630. [CrossRef]
22. Dodge, F.T.; Bowles, E.B. Draining of tanks with submerged outlets or without vacuum-relief. *J. Fluids Eng.* **1982**, *104*, 67–71. [CrossRef]
23. Sugioka, S.-I.; Kojima, T.; Nakata, K.; Horiguchi, F. Numerical Simulation of an Oil Spill in Tokyo Bay. *Spill Sci. Technol. Bull.* **1999**, *5*, 51–61. [CrossRef]
24. Tavakoli, M.T.; Amdahl, J.; Ashrafian, A.; Leira, B.H. Analytical Prediction of Oil Spill From Grounded Cargo Tankers. In Proceedings of the International Conference on Offshore Mechanics and Arctic Engineering, Estoril, Portugal, 15–20 June 2008; Volume 48197, pp. 911–920.
25. Goerlandt, F.; Montewka, J. A probabilistic model for accidental cargo oil out flow from product tankers in a ship-ship collision. *Mar. Pollut. Bull.* **2014**, *79*, 130–144. [CrossRef] [PubMed]
26. Kollo, M.; Laanearu, J.; Tabri, K. Hydraulic modelling of oil spill through submerged orifices in damaged ship hulls. *Ocean. Eng.* **2017**, *130*, 385–397. [CrossRef]
27. Chang, P.A.; Lin, C.W. *Hydrodynamic Analysis of Oil Outflow from Double Hull Tankers (CD-ROM)*; Naval Surface Warfare Center Carderock Division: Bethesda, MD, USA, 1994; pp. 25–26.
28. Ohtsubo, H.; Kawamoto, Y.; Kuroiwa, T. Experimental and numerical research on ship collision and grounding of oil tankers. *Nucl. Eng. Des.* **1994**, *150*, 385–396. [CrossRef]
29. Yamaguchi, K.; Yamanouchi, H. Oil spills from model tanks with double hull-IV. Effects of tank inclination on oil outflow. *J. Japan Inst. Navig.* **1996**, *94*, 291.

30. Simecek-Beatty, D.; Lehr, W.J.; Lankford, J. Leaking tank experiments for heavy oils. In Proceedings of the International Oil Spill Conference, American Petroleum Institute, Tampa, FL, USA, 25–29 March 2001; pp. 127–132.
31. Tavakoli, M.; Amdahl, J.; Leira, B.J. Experimental Investigation of Oil Leakage from Damaged Ships due to Collision and Grounding. *Ocean. Eng.* **2011**, *38*, 1894–1907. [CrossRef]
32. Bašića, J.; Degiulib, N.; Dejhallac, R. Total resistance prediction of an intact and damaged tanker with flooded tanks in calm water. *Ocean. Eng.* **2017**, *130*, 83–91. [CrossRef]
33. Lu, J.; Yang, Z.; Wu, H.; Wu, W.; Deng, J.; Yan, S. Effects of tank sloshing on submerged oil leakage from damaged tankers. *Ocean. Eng.* **2018**, *168*, 155–172. [CrossRef]
34. Cheng, L.Y.; Gomes, D.V.; Nishimoto, K. Simulação Computacional do Derramamento de Óleo eEstabilidade de um Petroleiro em Caso de Avaria. *Asoc. Argent. Mec. Comput.* **2010**, *29*, 7699–7710.
35. Tavakoli, M.T.; Amdahl, J.; Leira, B.J. Analytical and numerical modelling of oil spill from a side tank with collision damage. *Ships Offshore Struct.* **2012**, *7*, 73–86. [CrossRef]
36. Yang, H.; Yan, S.; Ma, Q.W. Effects of tank motions on oil spilling from damaged oil tanker. In Proceedings of the 26th International Ocean and Polar Engineering Conference, Rhodes, Greece, 26 June–1 July 2016; pp. 1–3.
37. Jeong, S.M.; Nam, J.W.; Park, J.C.; Youn, S.-M.; Kim, S.-Y. 2-D moving particle simulation on dynamic motion of a damaged ship with oil leaking in waves. In Proceedings of the OCEANS 2016 MTS/IEEE Monterey, Monterey, CA, USA, 19–23 September 2016; pp. 1–9.
38. Feng, X.; Liu, Y.; Wei, Q.; Su, J.; Zhang, D.; Zhou, Z.; Wu, W.; Xiong, C.; Peng, S. Numerical simulations on the oil plume evolutions and the two critical aspects of emergent oil containment for ship collision-incurred oil spills. *Ocean. Eng.* **2024**, *305*, 118030. [CrossRef]

**Disclaimer/Publisher's Note:** The statements, opinions and data contained in all publications are solely those of the individual author(s) and contributor(s) and not of MDPI and/or the editor(s). MDPI and/or the editor(s) disclaim responsibility for any injury to people or property resulting from any ideas, methods, instructions or products referred to in the content.